



A spectral-structural characterization of European temperate, hemiboreal and boreal forests

Miina Rautiainen¹, Arne Hovi¹, Daniel Schraik^{1,2}, Jan Hanuš³, Petr Lukeš³, Zuzana Lhotáková⁴, Lucie Homolová³

¹School of Engineering, Aalto University, Espoo, 00076, Finland

²Natural Resources Institute Finland, Helsinki, 00790, Finland

³CzechGlobe Global Change Research Institute of the Czech Academy of Sciences, Brno, 60300, Czech Republic

⁴Department of Experimental Plant Biology, Charles University, Prague, 12843, Czech Republic

Correspondence to: Miina Rautiainen (miina.a.rautiainen@aalto.fi)

Abstract. Radiative transfer models of vegetation play a crucial role in the development of remote sensing methods by providing a theoretical framework to explain how electromagnetic radiation interacts with vegetation in different spectral regions. A limiting factor in model development has been the lack of sufficiently detailed ground reference data on both structural and spectral characteristics of forests needed for testing and validating the models. In this data description paper, we present a dataset on the structural and spectral properties of 58 stands in temperate, hemiboreal and boreal European forests. It is specifically designed for the development and validation of radiative transfer models for forests but can also be utilized in other remote sensing studies. It comprises detailed data on forest structure based on forest inventory measurements, terrestrial and airborne laser scanning, and digital hemispherical photography. Furthermore, the data include spectral properties of the same forests at multiple scales: reflectance spectra of tree leaves and needles (based on laboratory measurements), forest floor (based on in situ measurements) and entire stands (based on airborne measurements), as well as transmittance spectra of tree leaves and needles and entire tree canopies (based on laboratory and in situ measurements, respectively). We anticipate that these data will have wide use in testing and validating radiative transfer models for forests and in the development of remote sensing methods for vegetation. The data can be accessed at:

Hovi et al. 2024a, <https://doi.org/10.23729/9a8d90cd-73e2-438d-9230-94e10e61adc9> (for laboratory and field data) and

Hovi et al. 2024b, <https://doi.org/10.23729/c6da63dd-f527-4ec9-8401-57c14f77d19f> (for airborne data).

1 Introduction

Remote sensing of vegetation, and forests in particular, has experienced significant growth in recent years due to advancements in sensor technology, data processing and interpretation techniques, and new satellite missions (e.g., Fassnacht et al., 2024). At a global level, remote sensing can provide information about pressing global issues such as the connections between climate change and vegetation dynamics (e.g., Piao et al., 2020) and support for biodiversity conservation (e.g., Pettorelli et al., 2016).



32 Furthermore, at finer spatial scales, optical remote sensing allows detailed and accurate monitoring of, for example, vegetation
33 productivity, diversity and health (e.g., Kooistra et al., 2024; Hernández-Clemente et al., 2019).

34 Radiative transfer (RT) models of vegetation play a crucial role in the development of remote sensing methods by providing a
35 theoretical framework to explain how electromagnetic radiation interacts with vegetation in different spectral regions (Ross,
36 1981; Myneni & Ross, 1991). Based on mathematical formulations, these models allow us to understand and quantify the
37 complex interactions between radiation and canopy components, such as leaves, and stems, and the underlying soil (Liang,
38 2004). By modeling the radiative transfer processes, it is possible to explain the spectral signatures observed by remote sensing
39 instruments under different environmental and illumination conditions, or support future sensor design and planning of data
40 collection strategies (e.g., Vicent et al., 2015).

41 RT models and other physically-based canopy reflectance and transmittance models have been developed for over three
42 decades. For forests, these models (e.g., Gastellu-Etchegorry et al., 1996; North, 1996; Kuusk & Nilson, 2000; Leblanc &
43 Chen, 2001) are often more complicated, and require a larger number of input variables than models for other vegetation
44 ecosystems (e.g., Jacquemoud et al. 2009; Verhoef et al., 1984) due to the complex tree canopy architecture and subsequent
45 multiple interactions of photons both within and between canopy elements, and between forest floor and the canopy (e.g.,
46 Stenberg et al., 2008). Even though there are modeling approaches that require a smaller number of input variables for forests
47 (Stenberg et al., 2016), a limiting factor in model development has been the lack of extensive or sufficiently detailed ground
48 reference data on both structural and spectral characteristics of forests needed for testing and validating the models. This lack
49 of data affects both model developers and larger scientific frameworks, such as the RADIATION transfer Model Intercomparison
50 (RAMI) initiative (Gobron et al., 2023). While structural data on forests (e.g., tree height, crown length, number of trees per
51 ground area, canopy cover, leaf area index) are commonly available from sources such as forest inventory databases, spectral
52 data on forest components (e.g., leaf or forest floor reflectance and/or transmittance spectra) are less frequently accessible. In
53 addition, some structural properties (e.g., clumping index) that are relevant for RT models are also not commonly available
54 but can be derived from detailed structural measurements.

55 To date, major efforts in collecting ground reference data that can be used in radiative transfer models for forests have focused
56 on the North American continent. For instance, projects like the National Ecological Observatory Network (NEON) (NEON,
57 2024) and the Boreal Ecosystem-Atmosphere Study (BOREAS) (Sellers et al., 1997) offer input data for developing RT
58 modeling for forests. While these initiatives have primarily aimed to understand ecosystem dynamics, their datasets also
59 include key variables needed for RT models. For testing and validating forest RT models in European forests, there is only a
60 small number of datasets that include the necessary structural and spectral information across various scales (e.g., Kuusk et
61 al., 2009; Widlowski et al., 2015; Schneider et al., 2017; Liu et al., 2023). Furthermore, these datasets are limited in size,
62 containing information on only a few forest stands. Even though various solutions have been suggested to overcome the lack
63 of input data for RT models by using data from multiple sources (e.g., Malenovský et al., 2019), the lack of missing primary



64 data persists. In addition to having to collect the data from multiple sources representing different time periods or geographical
65 locations, these datasets are often not openly available according to FAIR Data principles (Wilkinson et al., 2016).

66 In this data description paper, we present a unique, open dataset on the structural and spectral properties of 58 stands in
67 temperate, hemiboreal and boreal European forests collected in a project funded by the European Research Council. The
68 dataset is specifically designed for the development and validation of radiative transfer models for forests but can also be
69 utilized in other remote sensing studies. It comprises detailed information on forest structure based on forest inventory
70 measurements, terrestrial and airborne laser scanning, and digital hemispherical photography. Furthermore, the dataset
71 includes spectral properties of the forests at multiple scales: reflectance spectra of tree leaves and needles (based on laboratory
72 measurements), forest floor (based on in situ measurements) and entire stands (based on airborne measurements), as well as
73 transmittance spectra of tree leaves and needles and entire tree canopies (based on laboratory and in situ measurements,
74 respectively). For distributing the data, we selected open, widely available formats.

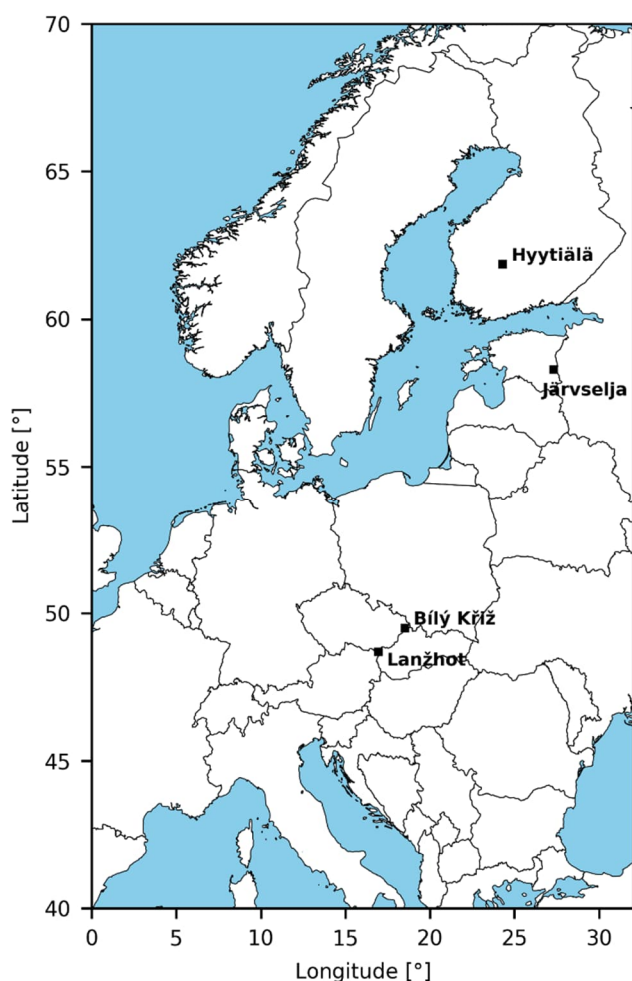
75



76 2 Data collection

77 2.1 Study sites

78 We collected data from 58 forest stands representing different forest structures and species compositions in temperate,
79 hemiboreal and boreal forests of Europe during summers 2019-2021 (Table 1, Fig. 1). The sites in Finland and the Czech
80 Republic (Hyytiälä, Lanžhot, Bílý Kříž) are part of the Integrated Carbon Observation System (ICOS) which means that time
81 series of meteorological and other ecosystem data are also openly available. The site in Estonia (Järvselja) also has a tower
82 system for measuring variables related to atmosphere-biosphere interactions, and the data are available, per request from the
83 tower manager. We have summarized information on the study sites in Table 1 and we provide a short verbal description of
84 them in the following text.



85

86 **Figure 1.** A map showing the locations of the study sites.



87 Our boreal study site was located in Finland, Hyytiälä (61°51'N, 24°18'E), and is a moderately flat (130–200 m a.s.l.) area
 88 dominated by coniferous tree species. The forest floor is dominated by dwarf shrubs, graminoids, mosses or lichens. Bare soil
 89 is rarely visible. Field measurements in Hyytiälä were conducted during 2019 and 2021.

90 Our hemiboreal site was located in Estonia, Järvelja (58°17'N, 27°19'E), and is a flat (30–45 m a.s.l.) area with mixed
 91 broadleaved and coniferous forests. The forest floor is dominated by shrubs, dwarf shrubs, graminoids and mosses. Bare soil
 92 is rarely visible. Field measurements in Järvelja were conducted during 2020.

93 Our temperate study sites, Lanžhot and Bílý Kříž, were located in the Czech Republic. Lanžhot (48°41'N, 16°57'E), is a
 94 temperate broadleaf-dominated floodplain forest area (ca 150 m a.s.l.). The forest floor is sparsely covered by graminoids and
 95 shrubs, and decomposed plant materials (or bare soil) is commonly visible due to a high game density. Bílý Kříž (49°30'N,
 96 18°32'E), on the other hand, is a temperate coniferous mountain forest area (700–950 m a.s.l.) where the forest floor is
 97 dominated by dwarf shrubs, graminoids and mosses. Field measurements in the Czech sites were conducted during 2019.

98

99 **Table 1.** Summary of the study plots and measurement campaigns.

	Hyytiälä	Järvelja	Bílý Kříž	Lanžhot
Forest biome	boreal	hemiboreal	temperate	temperate
Number of plots	28	13	7	10
Mean (and range) of tree height [m]	20 (6 – 34)	19 (4 – 39)	23 (5 – 43)	31 (18 – 40)
Mean basal area (and its range) [m ² ha ⁻¹]	23 (4 – 46)	19 (4 – 51)	34 (3 – 66)	33 (14 – 60)
Effective plant area index [m ² m ⁻²]	1.9 (0.1 – 3.9)	2.5 (0.4 – 6.3)	2.9 (0.4 – 4.7)	3.7 (2.1 – 5.3)
Time of field campaign	17 June – 26 July 2019, 8 July - 5 August 2021	24 June – 19 July 2020	16 – 29 September 2019	3 – 12 September 2019
Time of airborne campaign (date, local time)	13 July 2019, 08:57-10:21	15 July 2019, 12:57-14:07	4 September 2019, 11:01-11:07	4 September 2019, 12:14-12:22
Solar zenith angle during airborne measurements	51-60°	37-38°	47-48°	42°

100

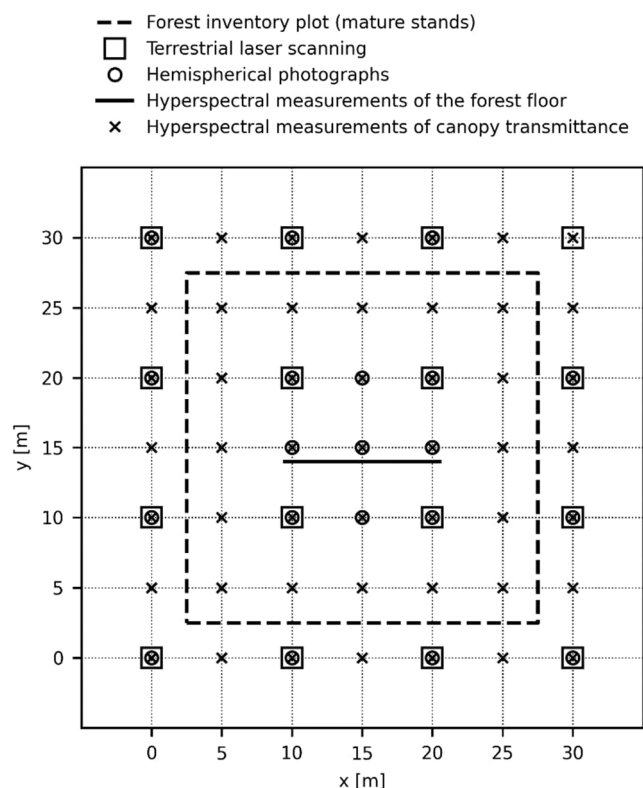


101 2.2 Overview of measurement campaigns

102 We established 28 plots in Hyytiälä, 13 in Järvelja, 10 in Lanžhot, and 7 in Bílý Kříž (Fig. 2). Each plot was located within a
103 homogeneous forest stand with a minimum distance of 30 m from the plot center to the stand border, to ensure that uncertainties
104 in geolocation would not impact the interpretation of commonly used medium spatial resolution optical satellite data. The
105 same sampling and measurement protocols were applied in collecting field data in all study sites.

106 In all plots, we carried out forest inventory (Sect. 2.3.1) and terrestrial laser scanning (Sect. 2.3.2), took hemispherical
107 photographs of the tree canopy (Sect. 2.3.3) and conducted spectral measurements and estimation of vegetation fractional
108 cover of the forest floor layer (Sect. 2.3.4). In addition, we measured the spectral transmittance of tree canopies in a subset of
109 plots (Sect. 2.3.5) and measured the reflectance and transmittance spectra of the foliage of dominant tree species in all study
110 sites (Sect. 2.3.6). An airborne measurement campaign in all study sites was conducted to obtain contemporaneous
111 hyperspectral (Sect. 2.4.1) and laser scanning data (Sect. 2.4.2). The same aircraft and instrumentation were used for the
112 acquisition of airborne data in all measurement campaigns. The datasets are provided by Hovi et al. 2024a and Hovi et al.
113 2024b.

114



115

116 **Figure 2.** A diagram showing the sampling design for field measurements described in Section 2.3.



117 2.3 Field datasets

118 2.3.1 Forest inventory

119 We conducted forest inventory measurements to obtain detailed information on the tree species and stand structure and took
120 photographs of each plot at six fixed locations to provide an overview of the forests for data users. Forest inventory was carried
121 out with distinct protocols for mature stands ($D > 10$ cm) and young stands ($D < 10$ cm), categorized based on the average
122 diameter at 1.3 m height (D) for trees. For simplicity, we refer to stands with $D > 10$ cm as mature stands and those with $D <$
123 10 cm as young stands.

124 In mature stands ($n = 44$), a tree-wise inventory was performed within a rectangular area measuring $25\text{ m} \times 25\text{ m}$ (Fig. 2). The
125 diameter at 1.3 m height was measured using a caliper, and the tree species were identified for every tree exceeding a
126 predetermined diameter threshold. The thresholds were determined in relation to the average tree height in the plot (h) and
127 were as follows: 8 cm if $h < 16$ m, 5 cm if $10\text{ m} \leq h \leq 16$ m, and 2.5 cm if $h < 10$ m. Tree height was measured with a Vertex
128 ultrasonic hypsometer for two trees (median trees of thickest 10% of trees) in each plot. These plots had 16 terrestrial laser
129 scanning (TLS) points (see Section 2.3.2).

130 In young stands ($n = 6$), 16 circular sub-plots were measured, arranged in a 4×4 grid with a 10 m distance between grid points
131 (see TLS grid in Fig. 2). The area of each sub-plot was 25 m^2 (i.e., had a radius of 2.82 m). Within each sub-plot, the number
132 of trees per species, along with the diameter and height of a median tree per species, were measured. These plots had one
133 terrestrial laser scanning (TLS) point (see Section 2.3.2).

134 An exception to the forest inventory protocol was made only in Hyytiälä for the plots ($n = 8$) measured in 2021, where relascope
135 sampling was used to determine whether a tree belonged to the plot or not. Diameter at 1.3 m height was measured for all
136 sampled trees, and tree height was measured for the median tree per species. These plots had one terrestrial laser scanning
137 (TLS) point (see Section 2.3.2).

138
139 Descriptive forest characteristics were derived from the forest inventory data for each study plot. These include: number of
140 stems per hectare, basal area, tree species proportions, and tree dimensions (i.e., stem diameter and tree height). More accurate
141 description of the calculation of these variables is provided in the readme file of the data.

142

143 2.3.2 Terrestrial laser scanning (TLS)

144 We collected TLS data that can be used to characterize the 3D geometry of the forest canopies in all plots, comprising a total
145 of ~2800 individual trees. The Leica P40 ScanStation, utilized in our study, operates at a wavelength of 1550 nm. It has a 6
146 mm beam diameter at the source and a 0.23 mrad beam divergence. The scan resolution equaled the beam divergence (i.e.,



147 0.23 mrad or around 0.013°). The only exceptions to this were the measurements 1) in Hyytiälä in 2021 (n = 8), and 2) in
148 young stands in Järvelja (n = 4) where the scan resolution was 0.31 mrad (0.018°). These exceptions are clearly labelled in
149 the dataset.

150 There were two alternative sampling strategies for collecting TLS data. The choice of sampling approach was based on stand
151 density at a height of 1-2 m above ground to avoid occlusion of co-registration targets, and time constraints. In 44 plots, TLS
152 scans were conducted at 16 grid points (Fig. 2), corresponding to the "mature" forest category described in Section 2.3.1. In
153 14 plots, TLS scans were conducted only at a single location (at the center of the plot, Fig. 2).

154 Scans were exclusively carried out under calm wind conditions (under 4 m s⁻¹ in 16-scan plots, under 8 m s⁻¹ in single scan
155 plots) and in dry weather. The scanning heights ranged from 1.4 to 1.8 m above the ground. In plots that had 16 scan positions,
156 co-registration of scans was done using 25 polystyrene sphere targets, mounted on 1.5-meter-tall sticks placed within the plot
157 area (Fig. 2). The co-registration errors were below 1 cm. All processing was done with the Leica Cyclone software.

158 The point clouds are intended for spatial modeling of canopy structure based on ray tracing rather than morphological
159 modeling. Therefore, no filtering was applied at any stage of the data processing to preserve information. The TLS data in
160 plots with 16 scans are available as full-resolution data, with each individual scan's point cloud stored separately, along with
161 the transformation parameters of the co-registration. For viewing purposes, we merged and downsampled the point clouds to
162 an average point spacing of 2 cm in Leica Cyclone, and cropped the plot to approximately a 35 m × 35 m area for the plots
163 that had 16 grid (scanning) points. For the single-scan plots, the downsampled point cloud includes all data. The downsampled
164 and merged point clouds are provided in the LAS format.

165

166 **2.3.3 Hemispherical photographs**

167 We also obtained a characterization of the tree canopies with hemispherical photography. Hemispherical photographs were
168 taken in each plot under diffuse illumination and windless or calm wind conditions with a Nikon D5000 digital camera
169 equipped with a geometrically calibrated lens (Sigma EX 4.5 mm f/2.8 DC HSM). The photographs were captured from 21
170 locations in each plot (Fig. 2) with the camera lens looking directly upwards. The camera was positioned at a height of 1.5 m
171 when the mean tree height in a stand was over 10 m, and at a height of 1.0 m in other forests.

172 The photographs were recorded in the best quality eight-bit JPEG format. We manually adjusted the exposure time based on
173 the illumination conditions and also took photographs with exposure times one stop higher and lower than the original, thus
174 doubling and halving the exposure time. In the processing of the photographs, we selected the one where the pixel values in
175 the blue band of the JPEG images filled the eight-bit dynamic range well without saturating the histogram, but also the other
176 photographs are included in the dataset.



177 These hemispherical photographs served as the basis for estimating effective plant area index (PAI_{eff}) and canopy gap fractions
178 in different view angles. Initially, the JPEG photographs were binarized according to Nobis and Hunziker (2005). Next,
179 effective PAI was calculated based on gap fractions determined for five concentric rings, each with median zenith angles of
180 10.7° , 23.7° , 38.1° , 52.8° , and 66.6° . This method closely followed the one presented in the manual of the LAI-2200 Plant
181 Canopy Analyzer (LI-COR 2012), with minor variations in the zenith angles (as listed above).

182

183 **2.3.4 Hyperspectral measurements and other characteristics of the forest floor**

184 We measured the spectral properties of the forest floor and estimated the fractional cover of different components forming the
185 forest floor in all plots. The composition of the forest floor ranged from nearly bare soil or litter to dense green vascular or
186 moss vegetation.

187 Hemispherical-conical reflectance factors (HCRF) of the forest floor (ranging from 350 to 2500 nm) were measured in a central
188 location in each plot using an Analytical Spectral Devices (ASD) FieldSpec4 spectrometer (serial number 18456) with a 25°
189 field-of-view. The initial spectral resolution ranged from 3 nm (for wavelengths ≤ 1000 nm) to 10 nm (for wavelengths > 1000
190 nm), the sampling interval was 1.4 nm and 1.1 nm for visible and near infrared (VNIR), and shortwave infrared (SWIR),
191 respectively, and the instrument interpolated and outputted the data at 1 nm intervals. Please note that the same details on
192 spectral resolution also apply to the data measured by the spectrometers described later in Sections 2.3.5 and 2.3.6.
193 Measurements were consistently conducted under diffuse illumination conditions, so that the influence of unstable illumination
194 conditions on the forest floor (i.e., sun flecks, shadows) could be avoided and the data collected at different latitudes and times
195 of the day would be comparable. Preparations for the measurements included a warming-up period for the spectrometer lasting
196 at least 30 minutes.

197 In each plot, we established a 11-meter-long East-West oriented transect and made a total of 15 measurements at approximately
198 80 cm intervals along it (Fig. 2). Measurements were recorded in the nadir direction from a height of approximately 1.3 m. For
199 calibration, white reference measurements of a 25 cm \times 25 cm Spectralon panel (with a nominal reflectance of 99%) were
200 conducted at both ends of the transect as well as at every third measurement point along the transect. Dark current
201 measurements were taken at both ends of the transect. The integration time, offset and gain of the spectrometer were adjusted
202 based on illumination conditions using automatic optimization.

203 Raw radiation signals (i.e., digital numbers, DN) were processed into hemispherical-conical reflectance factors (HCRF), and
204 the 15 pointwise measurements were averaged to produce a single spectrum per forest plot. We calculated the HCRF for each
205 measurement point by dividing the DN value of the forest floor by the DN value of the Spectralon panel and multiplied this
206 ratio with the reflectance of the white reference panel. Dark current readings were subtracted from all DN values prior to the
207 calculation. Because white reference readings were made at every third measurement point, we performed a linear interpolation



208 (in time) of the white reference measurements to obtain a value for all measurement points. The preprocessed data are provided
209 in the csv format.

210 Fractional cover was defined as the fraction of ground covered by living or dead plant material or lichens in 1 m² vegetation
211 quadrats. Fractional cover was estimated for all plots from nadir-view RGB (red, green, blue) photographs (four per plot) taken
212 by a Nikon D5000 camera at every fourth spectral measurement point (at a height of 1.5 m) along the transect where spectral
213 measurements were made. A wooden frame of 1 m × 1 m was placed at these measurement points, and the entire frame
214 (vegetation quadrat) was included in the photograph. After field work, the photographs were processed to obtain estimates of
215 fractional cover. The frame in each photograph was superimposed with a 10 × 10 grid, where each grid cell represented 1% of
216 the total image area. The forest floor present in each grid cell was visually classified into one of the following classes: 1)
217 vascular plants, 2) non-vascular plants (i.e., mosses), 3) lichen, 4) intact plant litter, or 5) decomposed plant litter. The criterion
218 for selecting one of the classes was that it was the most abundant class in the grid cell. Finally, the fractional cover of each
219 class in the photograph was determined by aggregating the grid cell specific results, and the average fractional cover of each
220 forest floor class within a forest plot was determined by calculating the mean of fractional cover values across the four
221 photographs.

222 **2.3.5 Hyperspectral measurements of canopy transmittance**

223 We conducted measurements of spectral transmittance of tree canopies (ranging from 350 to 2500 nm) in 8 plots in Hyytiälä,
224 6 plots in Järvelja, 4 plots in Lanžhot, and 4 plots in Bílý Kříž. Spectral transmittance of a canopy was defined as the ratio of
225 below-canopy spectral radiation flux to above-canopy spectral radiation flux.

226 For these measurements, we used two FieldSpec3 or -4 spectrometers and two identical cosine receptors (diffuser type, model
227 A124505) manufactured by ASD. In each forest plot, spectral transmittance was measured at 49 locations (Fig. 2). The ASD
228 FieldSpec4 spectrometer (serial number 18456) was consistently employed for measurements within the forest (i.e., below-
229 canopy), whereas the ASD FieldSpec3 or -4 (serial number 18641 or 16089) served as reference spectrometer (i.e., above-
230 canopy). For the above-canopy measurements, a tripod was used to affix the cosine receptor which was measuring at 15 second
231 intervals in an open area within the study site (within <2 km distance from the plots). Measurements were conducted only
232 under cloud-free conditions, with solar elevation angles ranging from 30° to 45°.

233 Preparations for the measurements included a warming-up period for the spectrometers lasting at least 30 minutes, automatic
234 optimization of the spectrometers' integration time and gain settings, and an intercalibration of the two spectrometers. The
235 intercalibration took place at the beginning and end of each measurement period (max 3 h 20 min). It involved placing the
236 cosine receptors next to each other in an open area and conducting ten measurements, with each measurement comprising 30
237 averaged spectra from both spectrometers.



238 After the field campaign, the data were processed into canopy spectral transmittance (T) as

$$239 \quad T = \frac{f_{bc}s_{bc}}{f_{ac}s_{ac}} k, \quad (1)$$

240 where s_{bc} and s_{ac} are raw signal (DN) values recorded below and above canopy, respectively, k is the ratio of DNs measured
241 by the two spectrometers under identical irradiance conditions (obtained from the intercalibration measurements), and f_{bc} and
242 f_{ac} are correction factors that take into account possible changes of the integration time (at wavelengths up to 1000 nm) or the
243 detector gain (at wavelengths above 1000 nm) due to re-optimization of either of the spectrometers during the measurement
244 period. Re-optimization was needed if signal saturation occurred, for example, when measuring before noon, as the solar
245 irradiance increased towards noon. All quantities in the equation are wavelength- or detector-dependent.

246 2.3.6 Hyperspectral measurements of tree leaves and needles

247 We measured the directional-hemispherical reflectance factors (DHRF) and directional-hemispherical transmittance factors
248 (DHTF) ranging from 350 to 2500 nm of leaves and needles for fifteen dominant tree species within the study sites, adding up
249 to a total of 1314 samples. The two coniferous tree species that we sampled were Norway spruce (*Picea abies* (L.) H. Karst.)
250 and Scots pine (*Pinus sylvestris* L.). The thirteen broadleaved tree species that we measured were common hazel (*Corylus*
251 *avellana* L.) English oak (*Quercus robur* L.), European alder (*Alnus glutinosa* (L.) Gaertn.), European ash (*Fraxinus excelsior*
252 L.), European aspen (*Populus tremula* L.), European hornbeam (*Carpinus betulus* L.), European Turkey oak (*Quercus cerris*
253 L.), goat willow (*Salix caprea* L.), hedge maple (*Acer campestre* L.), littleleaf linden (*Tilia cordata* Mill.), silver birch (*Betula*
254 *pendula* Roth), white poplar (*Populus alba* L.) and willows (*Salix* sp.). For simplicity, we will refer to leaves and needles
255 collectively as foliage in the following text.

256 The foliage samples were measured in laboratory conditions using ASD RTS-3ZC integrating spheres which were equipped
257 with a 10 W collimated halogen light source. The integrating sphere was coupled with an ASD spectrometer (FieldSpec3 serial
258 number 16089, or FieldSpec4 serial number 18456 or 18641). Preparations for the measurements included a warming-up
259 period for the spectrometer lasting at least 30 minutes.

260 In all study sites, visibly healthy foliage samples were obtained from both sun-exposed positions in the top-of-canopy and
261 shaded positions in the bottom-of-canopy using professional tree climbers, towers or long pruning shears. After cutting a
262 branch from the tree, it was stored in a cool environment (with a maximum storage time of 12 hours), maintained with adequate
263 watering, and foliage was removed from the branch immediately before the spectral measurements.

264 For coniferous trees, two age cohorts of needles were always sampled: current year (c0) and one-year-old (c1) needles. In
265 Hyytiälä, Järvelja and Bílý Kříž, three trees representing each tree species were sampled, with three samples collected for
266 each foliage class in each tree. This means that for all tree species, we sampled sun-exposed c0 and shaded c0 foliage samples,



267 and for conifers, we also sampled sun-exposed c1 and shaded c1 foliage classes. For less common broadleaved species in
268 Järvelja (European ash, goat willow, littleleaf linden, common hazelnut, and unspecified willow), samples from one tree were
269 obtained, and three sun-exposed c0 leaves were collected per tree species. In Lanžhot, one to four trees were selected for
270 sampling. Each tree contributed one sample for every foliage class, including shaded c0 or sun-exposed c0.

271 For the duration of the spectral measurement of a sample in Hyytiälä, Järvelja and Bílý Kříž, the sample (i.e., a leaf or a set
272 of 7-10 needles) was fixed in a custom-made sample holder (see Fig. 1 in Hovi et al., 2020 for sample holder design) that was
273 then fastened to the integrating sphere. Needles were arranged in the sample holder with a spacing of 0.5–1 times the width of
274 a single needle (as recommended by Yáñez-Rausell et al. 2014), and leaves were placed so that major veins were not included
275 in the measured spot. In Lanžhot, leaves of broadleaved species were not attached to sample holders.

276 We conducted measurements of DHRF and DHTF on both sides of the sample (corresponding to adaxial and abaxial in
277 broadleaved species), along with white reference measurements for both reflectance and transmittance. A photon trap was used
278 in the reflectance measurements to assess stray light. Our white reference was a Spectralon panel with 99% nominal
279 reflectance. The raw data were processed to derive leaf or needle DHRF and DHTF for all samples. For brevity, we denote
280 DHRF with R and DHTF with T in the following equations:

$$281 \quad R = \frac{s_R}{s_{ref,R}} \frac{1}{1 - P_{gap,R}} R_{ref}, \quad (2)$$

$$282 \quad T = \left(\frac{s_T}{s_{ref,T}} - P_{gap,T} \right) \frac{1}{1 - P_{gap,T}} R_{ref}, \quad (3)$$

283 where s_R and s_T represent the raw signals (DN) obtained from the reflectance and transmittance measurements. Similarly, $s_{ref,R}$
284 and $s_{ref,T}$ denote the DNs from the white reference measurements for reflectance and transmittance, respectively. R_{ref} indicates
285 the reflectance of the white reference panel, while $P_{gap,R}$ and $P_{gap,T}$ denote the gap fractions in the sample. Before R was
286 computed, stray light was first subtracted from s_R and $s_{ref,R}$.

287 For broadleaved species, the gap fraction was assigned a value of 0 in the above calculations. Coniferous samples, on the other
288 hand, included gaps between needles, and thus, we determined the gap fractions using a digital film scanner (Epson Perfection
289 V550, 800 dpi resolution). The detailed procedure for determination of gap fraction was done according to Hovi et al. (2020).
290 Finally, to address a slight inherent bias in transmittance measurements with the ASD RTS-3ZC integrating sphere (reported
291 by Hovi et al. 2020) and to ensure that the sum of DHRF and DHTF did not exceed one in the near-infrared (NIR) region, we
292 implemented an empirical correction in which the DHTF spectra were multiplied with a correction factor of 0.945.

293 For data users, we provide the spectra for all samples as well as analysis-ready datasets. The analysis-ready datasets contain i)
294 the mean DHRF and DHTF spectra and their standard deviations for all tree species, canopy positions (top and bottom), needle
295 age classes (c0, c1) and study sites, and ii) plot-specific mean DHRF and DHTF spectra which have been weighted based on
296 tree species and needle age class proportions (i.e., computed from i).



297 2.4 Airborne datasets

298 2.4.1 Hyperspectral data

299 We arranged flight campaigns in mid-July 2019 in Hyytiälä and Järvelja, and in early September 2019 in Lanžhot and Bílý
300 Kříž (Table 1), representing green phenological conditions. Airborne hyperspectral measurements were collected across all
301 study sites using the CASI-1500 and SASI-600 hyperspectral pushbroom sensors from Itres Ltd., Canada, mounted on a Cessna
302 C208B aircraft which is part of the Flying Laboratory of Imaging Systems (FLIS) operated by the CzechGlobe Global Change
303 Research Institute (Hanuš et al., 2023). The CASI-1500 covered visible (VIS) to NIR wavelengths (382 to 1052 nm), while
304 the SASI-600 sampled NIR and shortwave-infrared (SWIR) wavelengths (958 to 2443 nm). Both sensors had a sampling
305 interval and spectral resolution of 15 nm and underwent spectral and radiometric calibration prior to the flight campaigns in
306 March 2019.

307 During the flight campaigns, the aircraft flew at an altitude of approximately 1 km above ground level. This yielded ground
308 pixel sizes of 0.5 m (CASI) and 1.25 m (SASI). The CASI and SASI data were acquired in near-nadir observation geometry
309 with a +/- 20° field-of-view. The flying azimuth direction closely matched the solar azimuth – the purpose of this was to reduce
310 potential spectral differences within the same study site caused by reflectance anisotropy of forests in the solar principal plane.
311 During acquisitions, the Sun zenith angle ranged from 37° to 60°, and flight lines overlapped by 60–80%.

312 The raw DN data from the hyperspectral sensors underwent initial radiometric correction with the RadCor software (version
313 11) produced by Itres Ltd. Subsequently, geo-orthorectification was performed using GeoCor (version 5.6). The data were
314 orthorectified to a surface model, which represents the top-of-canopy in vegetated areas, and the ground elevation elsewhere.
315 Atmospheric correction was carried out with the ATCOR-4 software bundle (version 7.2.0 or 7.3.0), employing a database of
316 atmospheric look-up tables generated with the MODTRAN5 radiative transfer code. In this correction, sensor measurements
317 were adjusted for path and adjacency radiances. Inflight radiometric (vicarious) calibration was conducted for each site using
318 a known bright reflectance target. Spectral bands highly affected by water vapor in the atmosphere (i.e., 895-1003 nm, 1092-
319 1168 nm, 1302-1528 nm, and 1737-2038 nm) were nonlinearly interpolated and depended on local atmospheric conditions.
320 No topographic correction was applied. The data produced through this processing chain are provided as at-surface (also called
321 top-of-canopy) hemispherical-directional reflectance factors (HDRF).

322 Finally, we inspected the CASI and SASI data manually to remove clouds or cloud shadows from areas corresponding to our
323 study plots. During the flights, clouds were intermittently present over Hyytiälä site and occasionally in Bílý Kříž site. The
324 Lanžhot and Järvelja flights, on the other hand, had cloudless conditions. Nearest-to-nadir cloud-free data from a 100 m ×
325 100 m area around each plot were extracted and serve as an analysis-ready dataset. In addition, data from the entire study sites
326 are provided. These data cover approximately 4 km × 4 km areas in Hyytiälä and Järvelja, 2 km × 3 km in Lanžhot, and 2 km
327 × 2 km in Bílý Kříž.



328 2.4.2 Laser scanning data (ALS)

329 Airborne laser scanning (ALS) data were collected simultaneously with the airborne hyperspectral data using a Riegl LMS-
330 Q780 laser scanner (Riegl GmbH, Austria) mounted on the same Cessna aircraft. The laser scanner operated at a wavelength
331 of 1064 nm, had a 0.25 mrad beam divergence, and a maximum scan zenith angle of 30°. The pulse density at the study plots
332 was 48, 32, 10, and 9 pulses m⁻² in Hyytiälä, Järvelja, Lanžhot, and Bílý Kříž, respectively. The differences between sites
333 stem from different overlap of flight lines. In Hyytiälä, the elevated pulse density was also partly due to repeated flight lines
334 due to occasional cloud cover. The raw waveform data were processed into point cloud format using RiProcess (version 1.8.4),
335 RiAnalyze (version 6.2.2), RiWorld (version 5.1.3), and GeoSysManager (version 2.0.8) software. We also computed raster
336 digital elevation models with a pixel size of 1 m, by interpolating from the ground points classified with LASTools software.
337 Similarly to the airborne hyperspectral data, analysis-ready data were extracted for a 100 m × 100 m area around each study
338 plot, and the data are also provided for the entire study sites as original point clouds and denoised data. Denoised data were
339 processed to filter out points originating from the sky (due to e.g., clouds) or false points under ground.

340 2.5 External field datasets

341 Field datasets from other sources, and relevant to physically-based remote sensing but not included in our campaigns, are
342 available for the study sites. We have summarized these datasets in Table 2. They include 1) reflectance spectra of tree bark
343 for boreal and temperate tree species, 2) additional data sets on optical properties of Norway spruce needles from the Czech
344 study sites, and 3) forest meteorology, greenhouse gases, air quality and soil measurements from ICOS towers.

346 **Table 2.** Ancillary data sets relevant for RT modeling of forests available for the study sites from other projects.

Description of data set	Source
Stem bark reflectance spectra for boreal and temperate tree species	DOI: 10.17632/pwfxgzz5fj.2
Forest meteorology, greenhouse gases, air quality and soil measurements	
for Hyytiälä site	DOI: 10.23729/23dd00b2-b9d7-467a-9cee-b4a122486039
for Lanžhot site	https://meta.icos-cp.eu/objects/LaXYKv7nUEOYLD62wr43PK7H (last access 11 April 2024)
for Bílý Kříž site	https://meta.icos-cp.eu/objects/Ru01KATyDlvqFkOzvB7eBcrY (last access 11 April 2024)
Optical properties of Norway spruce needles	DOI: 10.17632/vycrxc4vpz.1

347



348 **3 Results**

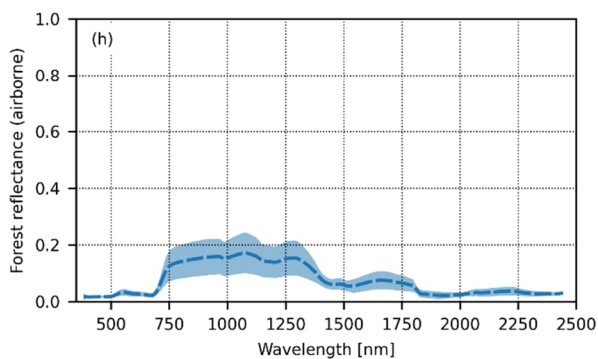
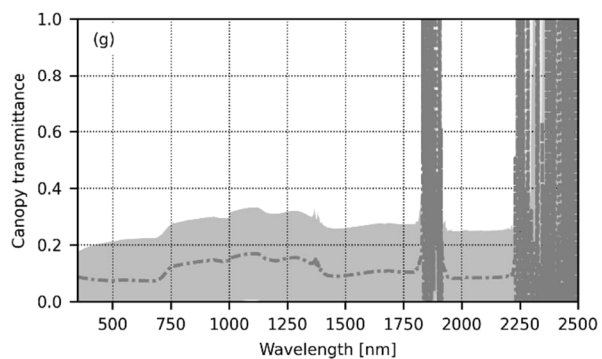
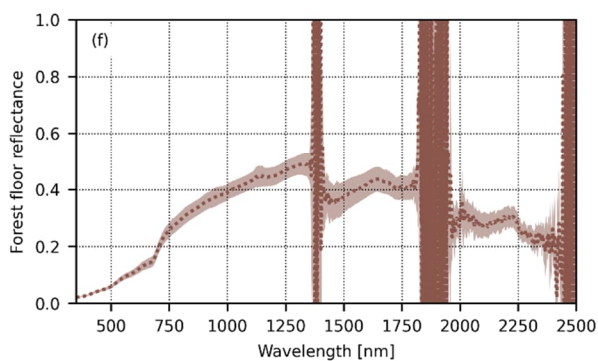
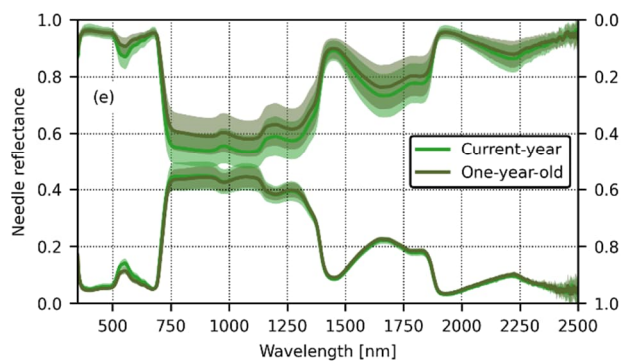
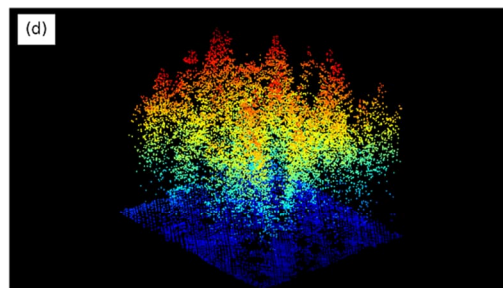
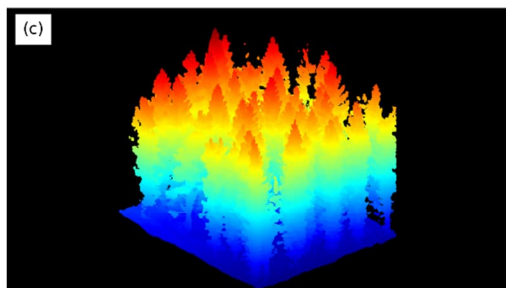
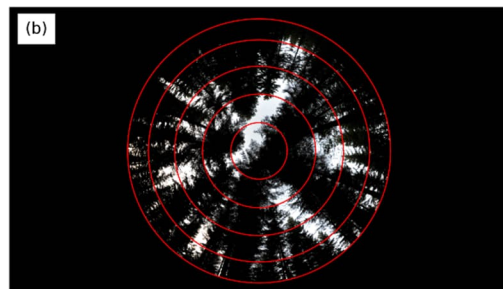
349 The data allow examining comprehensively the spectral and structural properties of forest stands. We summarized the different
350 data sources in two sets of figures, using a coniferous stand from Bílý Kříž (Fig. 3) and a broadleaved stand from Hyytiälä
351 (Fig. 4) as examples. These two forest stands illustrate the variation in structural and spectral properties both within and
352 between stands present in the new dataset. For example, the point clouds produced by laser scanning sensors and described in
353 this paper (Fig. 3c-d, 4c-d) can be used to visualize and compute canopy height distribution or density metrics, or to assess the
354 spatial distribution patterns of trees or foliage clumping in the study stands. The variation in the spectral properties of the study
355 stands, on the other hand, can be divided into several parts to examine tree leaf-level (Fig. 3e, Fig. 4e), forest floor level (Fig.
356 3f, Fig. 4f) and tree canopy level (Fig. 3g-h, Fig. 4g-h) phenomena. As a specific example of a key structural variable needed
357 in RT modeling of vegetation, we publish data on tree canopy gap fractions in different view angles based on hemispherical
358 photography. On average, in our coniferous stands, canopy gap fractions were approximately two times as high as in the
359 broadleaved stands, and in both types of forests, the gap fractions decreased linearly towards the horizon (Fig. 5).

360 Using the datasets described in this paper, differences in the spectral properties of forests can be investigated at multiple scales
361 (Fig. 6). In presenting the data here, we refer to the spectral regions as visible (~400–700 nm), near infrared (~700–1300 nm)
362 and shortwave infrared (~1300–2500 nm). In both coniferous and broadleaved stands, the reflectances were notably higher at
363 tree leaf level than at stand (canopy) level throughout the entire measured spectrum (Fig. 6a-b). Forest floor reflectances, on
364 the other hand, were usually lower than tree leaf level reflectances but higher than canopy level reflectances in the visible and
365 near-infrared regions. However, in the shortwave infrared region, the forest floor had, on average, a higher reflectance than
366 tree leaves or canopies in coniferous stands, and a reflectance similar to that of tree leaves in broadleaved stands (Fig. 6a-b).
367 An especially unique feature of this dataset is that also transmittance spectra at leaf and canopy levels were measured so that
368 they could be used in, for example, testing the performance of RT models. In our data, the canopy level spectral transmittance
369 of coniferous stands was more stable throughout the spectrum than the canopy level transmittance of broadleaved stands, and
370 that transmittances at leaf and canopy levels were usually lower in our coniferous study plots than in broadleaved study plots
371 (Fig. 6c-d). Furthermore, the data show that in the visible region, the spectral transmittance at canopy level was higher than
372 the spectral transmittance at leaf level. In the near-infrared and shortwave infrared regions, on the other hand, leaf level
373 transmittances were higher than canopy level transmittances. An exception to this was in the coniferous stands in two spectral
374 regions – around 1400–1500 nm and above ~1900 nm – where canopy level transmittances were again higher than leaf level
375 transmittances. In broadleaved stands, the canopy spectral transmittances in shortwave infrared were higher than leaf level
376 transmittances only in a small region around 1900–2000 nm.

377 Finally, the data also allow examining relationships between structural and spectral properties of forests through a combination
378 of contemporaneous airborne laser scanning and hyperspectral data (Fig. 7). These data can be used to illustrate, for example,
379 that, in the visible spectral region, forest reflectance decreased as a function of increasing canopy cover (defined as the first



380 echo cover index in ALS data) across forest stands representing different biomes (Figs. 7a, c), but that in the near-infrared and
381 shortwave infrared regions, broadleaved and coniferous stands with closed canopies (i.e., high canopy cover values) formed
382 two distinct groups so that coniferous stands had notably lower HDRFs than broadleaved stands did (Figs. 7e, g). Similar
383 phenomena were also observed in the relationships between forest reflectance and canopy height (defined as the 95th percentile
384 of all canopy echoes) obtained from ALS data (Fig. 7b, d, f, h).

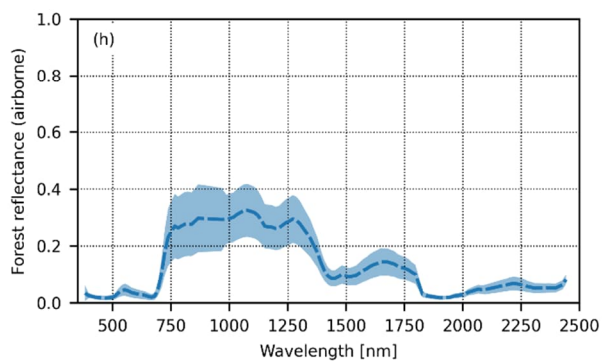
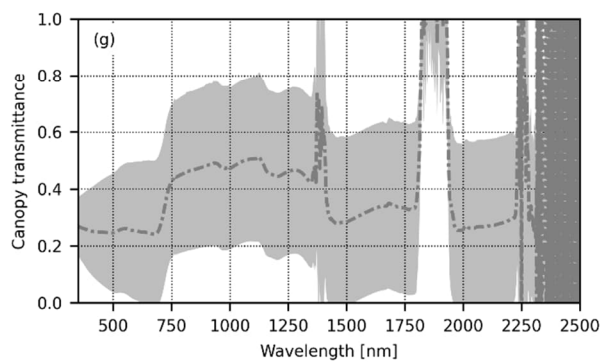
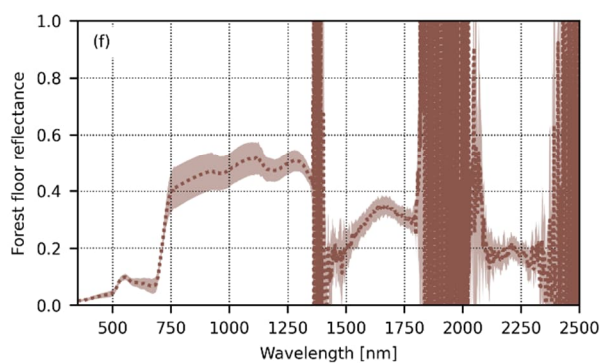
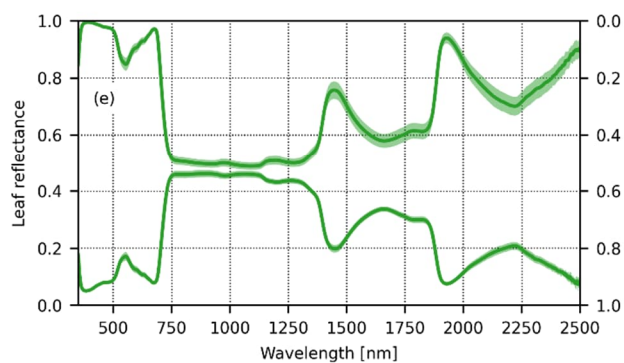
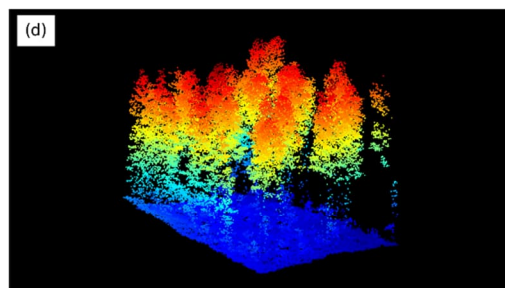
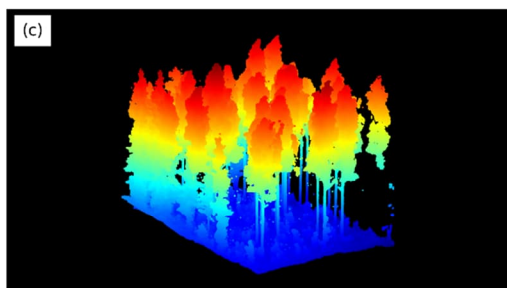
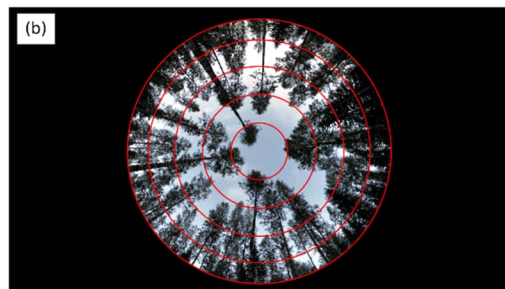


385

386 (figure caption on following page)



387 **Fig. 3.** A collection of figures summarizing the different types of data collected for a pure coniferous plot located in Bílý Kříž
388 (stand ID “BK_SPRUCE2” in the dataset). The dominant tree species is Norway spruce (99% of basal area), effective plant
389 area index 2.8, and mean tree height 20.8 m. **A.** An overview photograph of the plot (from the north-east corner towards the
390 plot center). **B.** A hemispherical photograph of the canopy (Section 2.3.3). **C.** Point cloud visualization of the plot based on
391 terrestrial laser scanning data from the south-west corner towards the plot center based on a downsampled point cloud (Section
392 2.3.2). **D.** Point cloud visualization of the plot based on airborne laser scanning data from the south-west corner towards the
393 plot center (from view zenith angle 45° , 17 pulses m^{-2}) (Section 2.4.2). **E.** Mean leaf-level reflectance and transmittance spectra
394 (DHRF and DHTF, respectively) and their standard deviations for current year and one-year-old needles of the dominant tree
395 species in the plot (Section 2.3.6). **F.** Mean reflectance spectrum (HCRF) and its standard deviation for the forest floor in the
396 plot (Section 2.3.4). Spectral regions with noise were caused by atmospheric water vapor. **G.** Mean spectral transmittance and
397 its standard deviation for the tree canopy layer (Section 2.3.5). Spectral regions with noise were mainly caused by atmospheric
398 water vapor, but also by the reduced sensitivity of the cosine receptor at the end of the spectral range ($>2200 \text{ nm}$). **H.** Mean
399 reflectance spectrum (HDRF) and its standard deviation for the entire plot ($25 \text{ m} \times 25 \text{ m}$ area) based on airborne measurements
400 (Section 2.4.1).

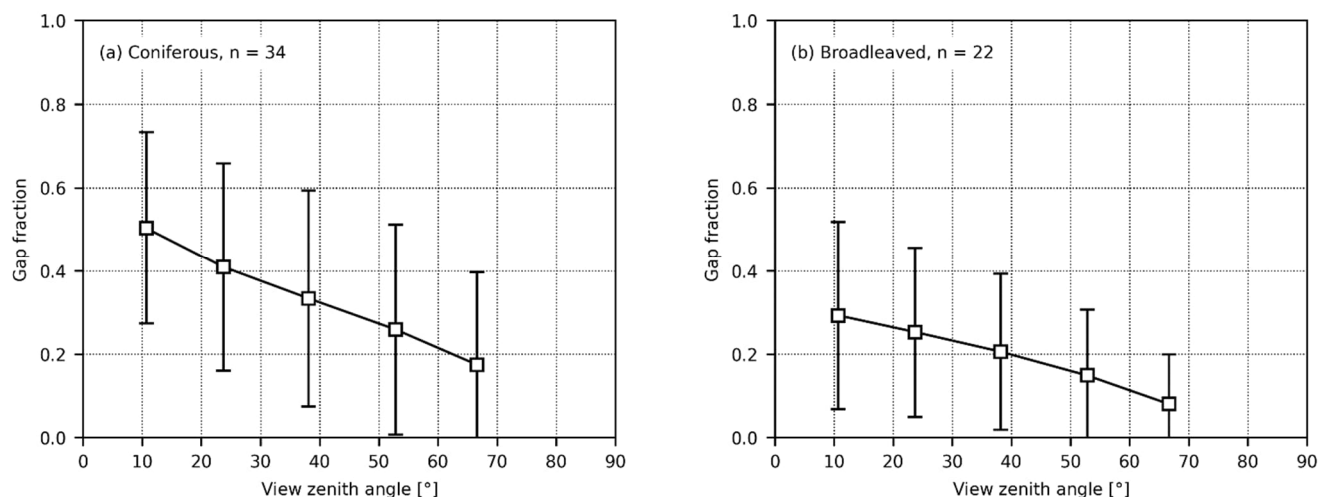


401

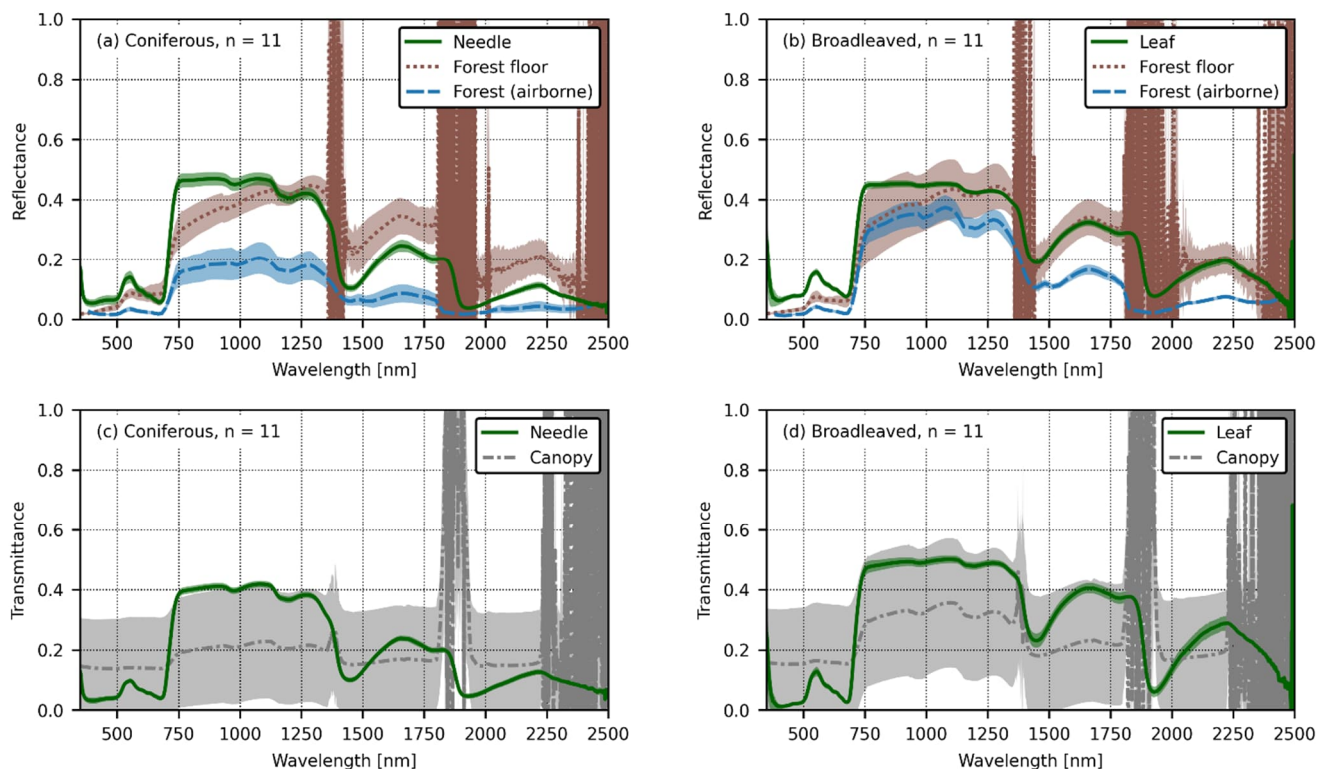
402 (figure caption on following page)



403 **Fig. 4.** A collection of figures summarizing the different types of data collected for a broadleaved plot located in Hyttiälä
404 (stand ID “HY_BIRCH2” in the dataset). The dominant tree species is silver birch (85% of basal area), effective plant area
405 index 1.5, and mean tree height 23.2 m. **A.** An overview photograph of the plot (from the north-west corner towards the plot
406 center). **B.** A hemispherical photograph of the canopy (Section 2.3.3). **C.** Point cloud visualization of the plot based on
407 terrestrial laser scanning data from the south-west corner towards the plot center based on a downsampled point cloud (Section
408 2.3.2). **D.** Point cloud visualization of the plot based on airborne laser scanning data from the south-west corner towards the
409 plot center (from view zenith angle 45° , 48 pulses m^{-2}) (Section 2.4.2). **E.** Mean leaf-level reflectance and transmittance spectra
410 (DHRF and DHTF, respectively) and their standard deviations for the dominant tree species in the plot (Section 2.3.6). **F.**
411 Mean reflectance spectrum (HCRF) and its standard deviation for the forest floor in the plot (Section 2.3.4). Spectral regions
412 with noise were caused by atmospheric water vapor. **G.** Mean spectral transmittance and its standard deviation for the tree
413 canopy layer (Section 2.3.5). Spectral regions with noise were mainly caused by atmospheric water vapor, but also by the
414 reduced sensitivity of the cosine receptor at the end of the spectral range ($>2200 \text{ nm}$). **H.** Mean reflectance spectrum (HDRF)
415 and its standard deviation for the entire plot ($25 \text{ m} \times 25 \text{ m}$ area) based on airborne measurements (Section 2.4.1).
416
417
418

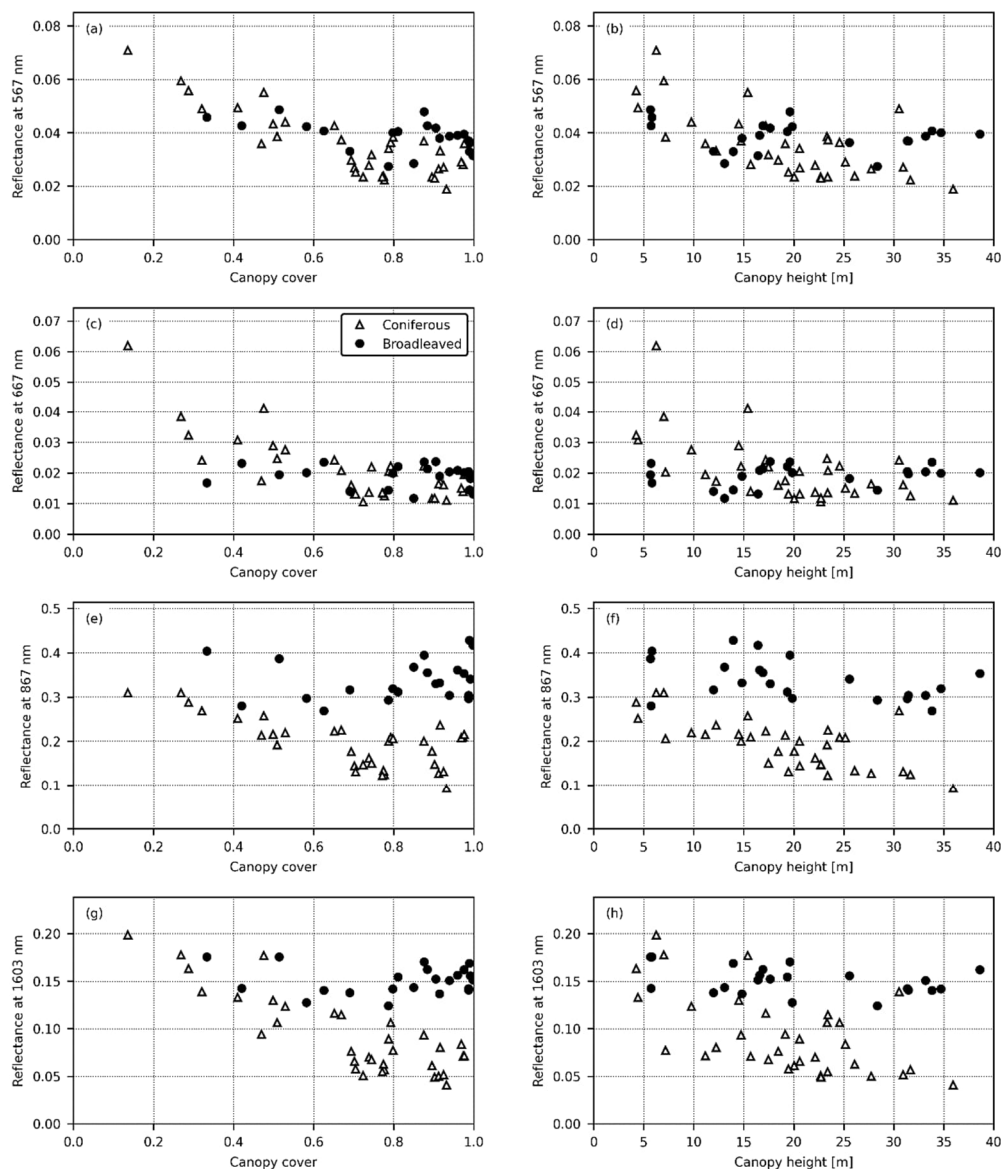


419
420 **Fig. 5.** Mean and standard deviation of canopy gap fractions in concentric view zenith angles as obtained from hemispherical
421 photographs in **A)** coniferous and **B)** broadleaved forests. Here, coniferous and broadleaved forests were defined so that at
422 least 75% of the trees (based on basal area) within the plot were coniferous or broadleaved species, respectively. The data
423 shown in this figure are based on measurements described in Section 2.2.3.



424

425 **Fig. 6.** Mean spectra at different scales. **A.** Mean reflectance spectra and their standard deviations for needles, forest floor and
426 entire forest plot in coniferous forests. **B.** Mean reflectance spectra and their standard deviations for leaves, forest floor and
427 entire forest plot in broadleaved forests. **C.** Mean transmittance spectra and their standard deviations for needles and canopies
428 in coniferous forests. **D.** Mean transmittance spectra and their standard deviations for needles and canopies in broadleaved
429 forests. The data shown in this figure are based on measurements and reflectance quantities described and defined in Sections
430 2.2.4-2.2.6 and 2.4.1., and only the subset of plots which had measurements of canopy transmittance are included here.
431 Coniferous and broadleaved forests were defined so that at least 75% of the trees (based on basal area) within the plot were
432 coniferous or broadleaved species, respectively. For visualization purposes, leaf-level reflectance and transmittance spectra
433 were first computed at plot-level as averages weighted by tree species proportions and needle age classes, and then averaged
434 over all plots to obtain the mean and standard deviation values shown in the above. Forest floor reflectance and canopy
435 transmittance data are shown with the noise that is inherently present in atmospheric water absorption bands in spectral data
436 measured outdoors. Forest reflectance (HDRF at plot-level, Fig. 6A and 6B) is averaged for an area of 25 m × 25 m in each
437 stand, and is based on airborne CASI and SASI data.



438

439

440

441

442

443

444

445

446

447

Fig. 7. The relationship between forest reflectance (HDRF, obtained from airborne CASI and SASI data) and forest structure (obtained from ALS data, scan zenith angle max 20°) for broadleaved and coniferous forests in four spectral regions: green (567 nm), red (667 nm), near-infrared (NIR, 867 nm) and shortwave infrared (SWIR, 1603 nm). The data are averaged for an area of 25 m × 25 m in each stand. Canopy cover was defined as the first echo cover index in ALS data, so that first echoes originating from the canopy were divided by all first echoes in the plot. **A. C. E. G.** Canopy cover and forest reflectance (HDRF). Spectral region indicated on the y-axis. **B. D. F. H.** Canopy height (defined as the 95th percentile of all canopy echoes in ALS data) and forest reflectance (HDRF). Spectral region indicated on the y-axis. Coniferous and broadleaved forests were defined so that at least 75% of the trees (based on basal area) within the plot were coniferous or broadleaved species, respectively. The data shown in this figure are based on measurements described in Section 2.4.



448 **4 Data availability**

449 The data are available in the open access repository Fairdata IDA which is a research data storage service provided by the
450 Ministry of Education and Culture of Finland. The data can be accessed at: Hovi et al. 2024a
451 <https://doi.org/10.23729/9a8d90cd-73e2-438d-9230-94e10e61adc9> (for data described in Section 2.3.) and Hovi et al. 2024b
452 <https://doi.org/10.23729/c6da63dd-f527-4ec9-8401-57e14f77d19f> (for data described in Section 2.4.).

453 **5 Conclusions**

454 Radiative transfer models of vegetation play a key role in advancing remote sensing science. The development of these models
455 has been hindered by a lack of comprehensive ground reference data on both the structural and spectral characteristics of
456 forests. In this paper, we introduced datasets containing information on the structural and spectral properties of temperate,
457 hemiboreal, and boreal European forest stands. We anticipate that these data will have wide use in testing and validating
458 radiative transfer models for forests and in other remote sensing studies beyond radiative transfer model development.

460 **Author contributions**

461 MR, AH and DS conceptualized the scientific data collection plan for the project. AH, DS, PL, ZL, LH and MR organized the
462 field campaigns and participated in data collection or processing. JH was responsible for organizing the airborne operations
463 and related data processing. AH curated the datasets and prepared data visualizations. MR prepared the manuscript with
464 contributions from all co-authors. MR was responsible for project administration and funding.

466 **Competing interests**

467 The contact author has declared that none of the authors has any competing interests.

469 **Acknowledgements**

470 We thank Juho Antikainen, Lucie Červená, Petri Forsström, Bijay Karki, Jussi Juola, Titta Majasalmi, Eva Neuwirthová, Ville
471 Ranta and Jaan Rönkkö for field work or data processing; Jan Pisek, Mait Lang, Mihkel Kaha and Andres Kuusk for support
472 in organizing the measurement campaign in Estonia; Jana Albrechtová for resources in organizing the field measurements in
473 the Czech Republic; Karel Holouš, Lukáš Fajmon and Tomáš Fabiánek for participation and support in airborne operations;
474 Lucie Hradecká and Ilari Lähteenmäki for advice in data management planning; and staff of all field stations of our study sites
475 for their help at different stages of the work.

477 **Financial support**

478 This study received funding from the European Research Council (ERC) under the European Union's Horizon 2020 research
479 and innovation programme (grant agreement No 771049 / Rautiainen). The text reflects only the authors' view and the Agency



480 is not responsible for any use that may be made of the information it contains. The work of the Czech scientists was made
481 possible by the Ministry of Education of the Czech Republic, project LTAUSA18154: Assessment of ecosystem function
482 based on Earth observation of vegetation quantitative parameters retrieved from data with high spatial, spectral and temporal
483 resolution, and the CzeCOS program, grant number LM2023048.

484

485 References

486

487 Fassnacht, F., White, J., Wulder, M. and Næsset, E.: Remote sensing in forestry: current challenges, considerations and
488 directions. *Forestry: An International Journal of Forest Research*, 97(1), 11–37, <https://doi.org/10.1093/forestry/cpad024>,
489 2024.

490 Gastellu-Etchegorry, J., Demarez, V., Pinel, V., and Zagolski, F.: Modeling radiative transfer in heterogeneous 3-D vegetation
491 canopies. *Remote Sensing of Environment*, 58, 131–156, [https://doi.org/10.1016/0034-4257\(95\)00253-7](https://doi.org/10.1016/0034-4257(95)00253-7), 1996.

492 Gobron, N., Lanconelli, C., Urraca Valle, R. and Govaerts, Y.: RAMI workshop – Radiative transfer modelling support to EO
493 metrology and Cal/Val activities. European Commission, Joint Research Centre, Publications Office of the European Union,
494 <https://data.europa.eu/doi/10.2760/23274>, last access: 11 April 2024.

495 Hanuš, J., Slezák, L., Fabiánek, T., Fajmon, L., Hanousek, T., Janoutová, R., Kopkáně, D., Novotný, J., Pavelka, K., Píkl, M.,
496 Zemek, F., and Homolová, L.: Flying Laboratory of Imaging Systems: Fusion of Airborne Hyperspectral and Laser Scanning
497 for Ecosystem Research. *Remote Sensing*, 15, 3130, <https://doi.org/10.3390/rs15123130>, 2023.

498 Hernández-Clemente, R., Homero, A., Möttus, M., Penuelas, J., González-Dugo, V., Jiménez, J., Suárez, L., Alonso, L., and
499 Zarco-Tejada, P.: Early Diagnosis of Vegetation Health From High-Resolution Hyperspectral and Thermal Imagery: Lessons
500 Learned From Empirical Relationships and Radiative Transfer Modelling, 5, 169–183, [https://doi.org/10.1007/s40725-019-](https://doi.org/10.1007/s40725-019-00096-1)
501 [00096-1](https://doi.org/10.1007/s40725-019-00096-1), 2019.

502 Hovi A., Möttus M., Juola J., Manoocheri F., Ikonen E., and Rautiainen M.: Evaluating the performance of a double integrating
503 sphere in measurement of reflectance, transmittance, and albedo of coniferous needles. *Silva Fennica*, 54(2), 10270.
504 <https://doi.org/10.14214/sf.10270>, 2020.

505 Hovi, A., Schraik, D., Hanuš, J., Lukeš, P., Lhotáková, Z., Homolová, L., and Rautiainen, M.: A spectral-structural
506 characterization of European temperate, hemiboreal and boreal forests: Airborne data. [https://doi.org/10.23729/c6da63dd-](https://doi.org/10.23729/c6da63dd-f527-4ec9-8401-57c14f77d19f)
507 [f527-4ec9-8401-57c14f77d19f](https://doi.org/10.23729/c6da63dd-f527-4ec9-8401-57c14f77d19f), 2024b.

508 Hovi, A., Schraik, D., Hanuš, J., Lukeš, P., Lhotáková, Z., Homolová, L., and Rautiainen, M.: A spectral-structural
509 characterization of European temperate, hemiboreal and boreal forests: Laboratory and field data.
510 <https://doi.org/10.23729/9a8d90cd-73e2-438d-9230-94e10e61adc9>, 2024a.

511 Jacquemoud, S., Verhoef, W., Baret, F., Bacour, C., Zarco-Tejada, P., Asner, G., François, C., and Ustin, S.: PROSPECT +
512 SAIL models: A review of use for vegetation characterization. 113, S1, S56–S66, <https://doi.org/10.1016/j.rse.2008.01.026>,
513 2009.

514 Kooistra, L., Berger, K., Brede, B., Graf, L. V., Aasen, H., Roujean, J.-L., Machwitz, M., Schlerf, M., Atzberger, C., Prikaziuk,
515 E., Ganeva, D., Tomelleri, E., Croft, H., Reyes Muñoz, P., Garcia Millan, V., Darvishzadeh, R., Koren, G., Herrmann, I.,
516 Rozenstein, O., Belda, S., Rautiainen, M., Rune Karlsen, S., Figueira Silva, C., Cerasoli, S., Pierre, J., Tanır Kayıkçı, E.,
517 Halabuk, A., Tunc Gormus, E., Fluit, F., Cai, Z., Kycko, M., Udelhoven, T., and Verrelst, J.: Reviews and syntheses: Remotely
518 sensed optical time series for monitoring vegetation productivity, *Biogeosciences*, 21, 473–511, [https://doi.org/10.5194/bg-](https://doi.org/10.5194/bg-21-473-2024)
519 [21-473-2024](https://doi.org/10.5194/bg-21-473-2024), 2024.

520 Kuusk, A., Kuusk, J. and Lang, M.: A dataset for the validation of reflectance models. *Remote Sensing of Environment*, 113(5),
521 889–892, <https://doi.org/10.1016/j.rse.2009.01.005>, 2009.

522 Kuusk, A. and Nilson, T.: A directional multispectral forest reflectance model. *Remote Sensing of Environment*, 72, 244–252,



- 523 [https://doi.org/10.1016/S0034-4257\(99\)00111-X](https://doi.org/10.1016/S0034-4257(99)00111-X), 2000.
- 524 Leblanc, S. and Chen, J.: A windows graphic user interface (GUI) for the five-scale model for fast BRDF simulations. *Remote Sensing Reviews*, 19, 293-305, <https://doi.org/10.1080/02757250009532423>, 2000.
- 525
- 526 Liang, S.: Canopy reflectance modeling. In: *Quantitative remote sensing of land surfaces*. Wiley, New Jersey, USA, 76-134, ISBN: 0-471-28166-2, 2004.
- 527
- 528 LI-COR 2012. LAI-2200 plant canopy analyzer instruction manual. LI-COR, Inc., publication number 984-10633, rev 2.
- 529 <https://www.licor.com/documents/6n3conpja6uj9aq1ruyn>, last access: 11 April 2024.
- 530 Malenovský, Z., Homolová, L., Lukeš, P., Buddenbaum, H., Verrelst, J., Alonso, L., Schaepman, M., Lauret, N. and
- 531 Gastellu-Etchegorry, J.: Variability and Uncertainty Challenges in Scaling Imaging Spectroscopy Retrievals and Validations
- 532 from Leaves Up to Vegetation Canopies. *Surveys in Geophysics*, 40, 631–656, <https://doi.org/10.1007/s10712-019-09534-y>,
- 533 2019.
- 534 Myneni, R. and Ross, J.: *Photon-vegetation interactions: Applications in optical remote sensing and plant ecology*. Springer-
- 535 Verlag, Berlin, Heidelberg, Germany. 565 pp., ISBN: 978-3-642-75391-6, 1991.
- 536 NEON (National Ecological Observatory Network): <https://www.neonscience.org/>, last access: 11 April 2024.
- 537 Nobis, M. and Hunziker, U.: Automatic thresholding for hemispherical canopy-photographs based on edge detection.
- 538 *Agricultural and Forest Meteorology*, 128(3-4), 243-250, <https://doi.org/10.1016/j.agrformet.2004.10.002>, 2005.
- 539 North, P.: Three-dimensional forest light interaction model using a Monte Carlo method. *IEEE Transactions on Geoscience*
- 540 *and Remote Sensing*, 34(4), 946 – 956, doi: [10.1109/36.508411](https://doi.org/10.1109/36.508411), 1996.
- 541 Pettorelli, N., Wegmann, M., Skidmore, A., Múcher, S., Dawson, T.P., Fernandez, M., Lucas, R., Schaepman, M.E., Wang,
- 542 T., O'Connor, B., Jongman, R.H.G., Kempeneers, P., Sonnenschein, R., Leidner, A.K., Böhm, M., He, K.S., Nagendra, H.,
- 543 Dubois, G., Fatoyinbo, T., Hansen, M.C., Paganini, M., de Klerk, H.M., Asner, G.P., Kerr, J.T., Estes, A.B., Schmeller, D.S.,
- 544 Heiden, U., Rocchini, D., Pereira, H.M., Turak, E., Fernandez, N., Lausch, A., Cho, M.A., Alcaraz-Segura, D., McGeoch,
- 545 M.A., Turner, W., Mueller, A., St-Louis, V., Penner, J., Vihervaara, P., Belward, A., Reyers, B. and Geller, G.N.: Framing the
- 546 concept of satellite remote sensing essential biodiversity variables: challenges and future directions. *Remote Sensing in*
- 547 *Ecology and Conservation*, 2(3), 122-131, <https://doi.org/10.1002/rse2.15>, 2016.
- 548 Piao, S., Wang, X., Park, T., Chen C., Lian, X., He, Y., Bjerke, J., Chen, A., Ciais, P., Tommervik, H., Nemani, R. and Myneni,
- 549 R.: Characteristics, drivers and feedbacks of global greening. *Nature Reviews Earth & Environment*, 1, 14–27,
- 550 <https://doi.org/10.1038/s43017-019-0001-x>, 2020.
- 551 Ross, J.: *The radiation regime and architecture of plant stands*. Kluwer Academic Publishers, The Hague, the Netherlands, 391
- 552 pp., ISBN: 9061936071, 1981.
- 553 Schneider, F.D., Morsdorf, F., Schmid, B., Petchey, O., Hueni, A., Schimel, D. and Schaepman, M.: Mapping functional
- 554 diversity from remotely sensed morphological and physiological forest traits. *Nature Communications*, 8:1441.
- 555 <https://doi.org/10.1038/s41467-017-01530-3>, 2017.
- 556 Sellers, P., Hall, F., Kelly, R., Black, A., Baldocchi, D., Berry, J., Ryan, M., Ranson, J., Crill, P., Lettenmaier, D.,
- 557 Margolis, H., Cihlar, J., Newcomer, J., Fitzjarrald, D., Jarvis, P., Gower, S., Halliwell, D., Williams, D., Goodison, B.,
- 558 Wickland, D. and Guertin, F.: BOREAS in 1997: Experiment overview, scientific results, and future directions. *Journal of*
- 559 *Geophysical Research: Atmospheres*, 102(D24), 28731-28769, <https://doi.org/10.1029/97JD03300>, 1997.
- 560 Stenberg, P., Möttus, M. and Rautiainen, M.: Modeling the spectral signature of forests: application of remote sensing models
- 561 to coniferous canopies. In (Ed. S. Liang): *Advances in Land remote Sensing: System, Modeling, Inversion and Application*.
- 562 Springer-Verlag, 147-171, ISBN: 978-1-4020-6449-4, 2008.
- 563 Stenberg, P., Möttus, M. and Rautiainen, M.: Photon recollision probability in modelling the radiation regime of canopies —
- 564 A review. *Remote Sensing of Environment*, 183, 98-108, <https://doi.org/10.1016/j.rse.2016.05.013>, 2016.
- 565 Verhoef, W.: Light scattering by leaf layers with application to canopy reflectance modeling: The SAIL model. *Remote*
- 566 *Sensing of Environment*, 16(2), 125-141, [https://doi.org/10.1016/0034-4257\(84\)90057-9](https://doi.org/10.1016/0034-4257(84)90057-9), 1984.



- 567 Vicent, J., Sabater, N., Tenjo, C., Acarreta, J., Ramón, J., Manzano, M., Rivera, J. Jurado, P. Franco, R. Alonso, L., Verrelst,
568 J., and Moreno, J.: FLEX End-to-End Mission Performance Simulator. IEEE Transactions on Geoscience and Remote Sensing,
569 54(7), 4215-4223. doi: [10.1109/TGRS.2016.2538300](https://doi.org/10.1109/TGRS.2016.2538300), 2015.
- 570 Widlowski, J.-L., Mio, C., Disney, M., Adams, J., Andredaki, I., Atzberger, C., Brennan, J., Busetto, L., Chelle, M.,
571 Ceccherini, G., Colombo, R., Côté, J.-F., Eemäe, A., Essery, R., Gastellu-Etchegorry, J. P., Gobron, N., Grau, E., Haverd, V.,
572 Homolová, L., Huang, H., Hunt, L., Kobayashi, H., Koetz, B., Kuusk, A., Kuusk, J., Lang, M., Lewis, P., Lovell, J. L.,
573 Malenovsky, Z., Meroni, M., Morsdorf, F., Möttus, M., Ni-Meister, W., Pinty, B., Rautiainen, M., Schlerf, M., Somers, B.,
574 Stuckens, J., Verstraete, M. M., Yang, W., Zhao, F. and Zenone, T.: The fourth phase of the radiative transfer model
575 intercomparison (RAMI) exercise: Actual canopy scenarios and conformity testing. Remote Sensing of Environment, 169,
576 418-437, <https://doi.org/10.1016/j.rse.2015.08.016>, 2015.
- 577 Wilkinson, M.D., Dumontier, M., Aalbersberg, I.J.J., Appleton, G., Axton, M., Baak, A., Blomberg, N., Boiten, J.-W., Da
578 Silva Santos, L.B., Bourne, P.E., Bouwman, J., Brookes, A.J., Clark, T., Crosas, M., Dillo, I., Dumon, O., Edmunds, S., Evelo,
579 C.T., Finkers, R., Gonzalez-Beltran, A., Gray, A.J.G., Groth, P., Goble, C., Grethe, J.S., Heringa, J., Hoen, P.A.C., Hooft, R.,
580 Kuhn, T., Kok, R., Kok, J., Lusher, S.J., Martone, M.E., Mons, A., Packer, A.L., Persson, B., Rocca-Serra, P., Roos, M., Van
581 Schaik, R., Sansone, S.-A., Schultes, E., Sengstag, T., Slater, T., Strawn, G., Swertz, M.A., Thompson, M., Van Der Lei, J.,
582 Van Mulligen, E., Velterop, J., Waagmeester, A., Wittenburg, P., Wolstencroft, K., Zhao, J. and Mons, B.: The FAIR Guiding
583 Principles for scientific data management and stewardship. Scientific Data, 3, 160018. <https://doi.org/10.1038/sdata.2016.18>,
584 2016.
- 585 Yáñez-Rausell, L., Schaepman, S., Clevers, J. and Malenovsky, Z.: Minimizing Measurement Uncertainties of Coniferous
586 Needle-Leaf Optical Properties, Part I: Methodological Review. IEEE Journal of Selected Topics in Applied Earth
587 Observations and Remote Sensing, 7(2), 399-405, doi: [10.1109/JSTARS.2013.2272890](https://doi.org/10.1109/JSTARS.2013.2272890), 2014.